# Reconstruction of wave front and object for inline holography from a set of detection planes

J. Hagemann, A. -L. Robisch, D. R. Luke, C. Homann, T. Hohage, P. Cloetens, H. Suhonen, T. Salditt

# Reconstruction of wave front and object for inline holography from a set of detection planes

**J. Hagemann,[1] A.-L. Robisch,[1] D. R. Luke,[2] C. Homann,[2] T. Hohage,[2] P. Cloetens,[3] H. Suhonen,[3] and T. Salditt[1]***

[1] *Institute for X-ray Physics, Georg-August-University Göttingen, Germany*
[2] *Institute for Numerical and Applied Mathematics, Georg-August-University Göttingen, Germany*
[3] *European Synchrotron Radiation Facility, Grenoble, France*
*tsaldit@gwdg.de*

**Abstract:** We illustrate the errors inherent in the conventional empty beam correction of full field X-ray propagation imaging, i.e. the division of intensities in the detection plane measured with an object in the beam by the intensity pattern measured without the object, i.e. the empty beam intensity pattern. The error of this conventional approximation is controlled by the ratio of the source size to the smallest feature in the object, as is shown by numerical simulation. In a second step, we investigate how to overcome the flawed empty beam division by simultaneous reconstruction of the probing wavefront (probe) and of the object, based on measurements in several detection planes (multi-projection approach). The algorithmic scheme is demonstrated numerically and experimentally, using the defocus wavefront of the hard X-ray nanoprobe setup at the European Synchrotron Radiation Facility (ESRF).



**OCIS codes:** (340.7440) X-ray imaging; (100.5070) Phase retrieval.

## References and links

1. P. Cloetens, W. Ludwig, J. Baruchel, D. van Dyck, J. van Landuyt, J. Guigay, and M. Schlenker, "Holotomography: Quantitative phase tomography with micrometer resolution using hard synchrotron radiation x rays," Appl. Phys. Lett. **75**, 2912–2914 (1999).
2. D. M. Paganin, *Coherent x-ray optics* (New York: Oxford University Press, 2006).
3. K. A. Nugent, "The measurement of phase through the propagation of intensity: An introduction," Contemp. Phys. **52**, 55–69 (2011).
4. H. M. Quiney, "Coherent diffractive imaging using short wavelength light sources," J. Mod. Opt. **57**, 1109–1149 (2010).
5. D. R. Luke, J. V. Burke, and R. G. Lyon, "Optical wavefront reconstruction: Theory and numerical methods," SIAM Rev. **44**, 169–224 (2002).
6. T. E. Gureyev and K. A. Nugent, "Rapid quantitative phase imaging using the transport of intensity equation," Opt. Commun. **133**, 339–346 (1997).
7. M. Krenkel, M. Bartels, and T. Salditt, "Transport of intensity phase reconstruction to solve the twin image problem in holographic x-ray imaging," Opt. Express **21**, 2220–2235 (2013).
8. E. Maire, J.-Y. Buffière, L. Salvo, J. J. Blandin, W. Ludwig, and J. M. Letang, "On the application of x-ray microtomography in the field of materials science," Adv. Eng. Mater. **3**, 539–546 (2001).
9. P. Tafforeau, R. Boistel, E. Boller, A. Bravin, M. Brunet, Y. Chaimanee, P. Cloetens, M. Feist, J. Hoszowska, and J.-J. Jaeger, "Applications of x-ray synchrotron microtomography for non-destructive 3D studies of paleontological specimens," Appl. Phys. A Mater. **83**, 195–202 (2006).

#203649 - $15.00 USD Received 10 Jan 2014; revised 25 Mar 2014; accepted 30 Mar 2014; published 6 May 2014

10. B. D. Metscher, "Biological applications of x-ray microtomography: Imaging microanatomy, molecular expression and organismal diversity," Microsc. Anal. (Am Ed) **27**, 13–16 (2013).
11. T. van de Kamp, P. Vagovič, T. Baumbach, and A. Riedel, "A biological screw in a beetle's leg," Science **333**, 52–52 (2011).
12. J. Moosmann, A. Ershov, V. Altapova, T. Baumbach, M. S. Prasad, C. LaBonne, X. Xiao, J. Kashef, and R. Hofmann, "X-ray phase-contrast in vivo microtomography probes new aspects of xenopus gastrulation," Nature **497**, 374 – 377 (2013).
13. M. Bartels, V. H. Hernandez, M. Krenkel, T. Moser, and T. Salditt, "Phase contrast tomography of the mouse cochlea at microfocus x-ray sources," Appl. Phys. Lett. **103**, 083703 (2013).
14. A. Pogany, D. Gao, and S. W. Wilkins, "Contrast and resolution in imaging with a microfocus x-ray source," Rev. Sci. Instrum. **68**, 2774–2782 (1997).
15. P. Cloetens, R. Mache, M. Schlenker, and S. Lerbs-Mache, "Quantitative phase tomography of Arabidopsis seeds reveals intercellular void network," Proc. Natl. Acad. Sci. USA **103**, 14626–14630 (2006).
16. M. Bartels, M. Priebe, R. Wilke, S. Kruger, K. Giewekemeyer, S. Kalbfleisch, C. Olendrowitz, M. Sprung, and T. Salditt, "Low-dose three-dimensional hard x-ray imaging of bacterial cells," Opt. Nanoscopy, 1-10 (2012).
17. K. Giewekemeyer, S. Krüger, S. Kalbfleisch, M. Bartels, C. Beta, and T. Salditt, "X-ray propagation microscopy of biological cells using waveguides as a quasipoint source," Phys. Rev. A **83**, 023804 (2011).
18. C. Olendrowitz, M. Bartels, M. Krenkel, A. Beerlink, R. Mokso, M. Sprung, and T. Salditt, "Phase-contrast x-ray imaging and tomography of the nematode Caenorhabditis elegans," Phys. Med. Biol. **57**, 5309–5323 (2012).
19. G. Martinez-Criado, R. Tucoulou, P. Cloetens, P. Bleuet, S. Bohic, J. Cauzid, I. Kieffer, E. Kosior, S. Laboure, S. Petitgirard, A. Rack, J. A. Sans, J. Segura-Ruiz, H. Suhonen, J. Susini, and J. Villanova, "Status of the hard x-ray microprobe beamline ID22 of the European Synchrotron Radiation Facility," J. Synchrotron Radiat. **19**, 10–18 (2012).
20. S. Kalbfleisch, H. Neubauer, S. P. Krüger, M. Bartels, M. Osterhoff, D. D. Mai, K. Giewekemeyer, B. Hartmann, M. Sprung, and T. Salditt, "The Göttingen holography endstation of beamline P10 at PETRA III/DESY," AIP Conf. Proc. **1365**, 96–99 (2011).
21. R. Barrett, R. Baker, P. Cloetens, Y. Dabin, C. Morawe, H. Suhonen, R. Tucoulou, A. Vivo, and L. Zhang, "Dynamically-figured mirror system for high-energy nanofocusing at the ESRF," Proc. SPIE pp. 813904–813912 (2011).
22. K. Giewekemeyer, "A study on new approaches in coherent x-ray microscopy of biological specimens," Ph.D. thesis, Universität Göttingen (2011).
23. P. Thibault, M. Dierolf, O. Bunk, A. Menzel, and F. Pfeiffer, "Probe retrieval in ptychographic coherent diffractive imaging," Ultramicroscopy **109**, 338–343 (2009).
24. A. M. Maiden and J. M. Rodenburg, "An improved ptychographical phase retrieval algorithm for diffractive imaging," Ultramicroscopy **109**, 1256–1262 (2009).
25. M. Stockmar, P. Cloetens, I. Zanette, B. Enders, M. Dierolf, F. Pfeiffer, and P. Thibault, "Near-field ptychography: Phase retrieval for inline holography using a structured illumination," Sci. Rep. **3**, 1–6 (2013).
26. H. M. Quiney, A. G. Peele, Z. Cai, D. Paterson, and K. A. Nugent, "Diffractive imaging of highly focused x-ray fields," Nature **2**, 101–104 (2006).
27. F. Döring, A.-L. Robisch, C. Eberl, M. Osterhoff, A. Ruhlandt, T. Liese, F. Schlenkrich, S. Hoffmann, M. Bartels, T. Salditt, and H. U. Krebs, "Sub-5 nm hard x-ray point focusing by a combined Kirkpatrick-Baez mirror and multilayer zone plate," Opt. Express **21**, 19311–19323 (2013).
28. T. B. Edo, D. J. Batey, A. M. Maiden, C. Rau, U. Wagner, Z. D. Pešić, T. A. Waigh, and J. M. Rodenburg, "Sampling in x-ray ptychography," Phys. Rev. A **87**, 053850 (2013).
29. D. L. Misell, "An examination of an iterative method for the solution of the phase problem in optics and electron optics: I. Test calculations," J. Phys. D: Appl. Phys. **6**, 2200–2216 (1973).
30. B. M. Hanser, M. G. L. Gustafsson, D. A. Agard, and J. W. Sedat, "Phase-retrieved pupil functions in wide-field fluorescence microscopy," J. Microsc. **216**, 32–48 (2004).
31. L. J. Allen, W. McBride, and M. P. Oxley, "Exit wave reconstruction using soft x-rays," Opt. Commun. **233**, 77–82 (2004).
32. L. J. Allen, W. McBride, N. O'Leary, and M. P. Oxley, "Exit wave reconstruction at atomic resolution," Ultramicroscopy **100**, 91–104 (2004).
33. D. R. Luke, "Relaxed averaged alternating reflections for diffraction imaging," Inverse Probl. **21**, 37–50 (2005).
34. S. C. Kramer and J. Hagemann, "SciPAL: Expression templates and composition closure objects for high performance computational physics with CUDA and OpenMP," ACM Trans. on Parallel Comput. (submitted).
35. J. N. Clark, C. T. Putkunz, M. A. Pfeifer, A. G. Peele, G. J. Williams, B. Chen, K. A. Nugent, C. Hall, W. Fullagar, S. Kim, and I. McNulty, "Use of a complex constraint in coherent diffractive imaging," Opt. Express **18**, 1981–1993 (2010).
36. L. J. Allen, H. M. L. Faulkner, K. A. Nugent, M. P. Oxley, and D. Paganin, "Phase retrieval from images in the presence of first-order vortices," Phys. Rev. E **63**, 037602 (2001).
37. L. J. Allen and M. P. Oxley, "Phase retrieval from series of images obtained by defocus variation," Opt. Commun. **199**, 65–75 (2001).

#203649 - $15.00 USD Received 10 Jan 2014; revised 25 Mar 2014; accepted 30 Mar 2014; published 6 May 2014

38. A.-L. Robisch and T. Salditt, "Phase retrieval for object and probe using a series of defocus near-field images," Opt. Express **21**, 23345–23357 (2013).
39. C. Homann, J. Hagemann, T. Salditt, and T. Hohage, "Remarks on the product approximation in the detector plane," (in prepartion).

## 1. Introduction

X-ray propagation full field imaging and tomography have become powerful imaging techniques, based on successful development of phase retrieval algorithms [1–5]. In the detection plane, the contrast for both absorbing and phase shifting features is generated by the inherent near-field diffraction behind a sample which is illuminated (probed) by an extended x-ray wavefront $P$ of sufficiently high spatial coherence. The exit wavefront and hence the complex-valued sample transmission function of the object $O$ can be reconstructed from the intensity distribution in the detection plane at some (defocus) distance $z$ behind the object plane, based, for example, on the transport-of-intensity equation (TIE) or various iterative algorithms [1, 6, 7]. A wide spectrum of applications ranging from material science [8], paleontology [9], histology [10], small arthropod biology [11] has emerged, taking advantage of the unprecedented 3D imaging capability, including fast tomography applications of dynamic processes [12]. While this development has been driven by the brilliance and coherence of synchrotron radiation, to some extent the method can be translated to compact laboratory-scale $\mu$-CT instruments, preserving fully quantitative reconstruction [13]. Furthermore, in order to achieve higher spatial resolution, propagation imaging and tomography can be extended from the parallel beam case to quasi-spherical beams, allowing for adjustable geometric magnification [14–16]. With this approach, projection micrographs and tomograms of biological cells [16, 17], tissues and small organisms [18] can be recorded with quantitative density contrast and pixel size below 50 nm.

The necessary diverging spherical wavefronts for high magnification are created by nanofocus x-ray optics, such as Kirkpatrick-Baez (KB) mirror systems [19, 20]. For such optical systems, already small imperfections like mirror figure errors result in strong phase aberrations due to the small wavelength of x-rays [21]. The empty beam far-field patterns are therefore strongly affected and never correspond to the clean homogeneous flat field distribution ideally assumed. This aberrated empty beam, however, constitutes the probing field $P$ for $O$. According to current wisdom, the problem is dealt with by simple division of the recorded image with object by that of the empty beam [17, 22]. In fact, the raw images are hardly ever presented in publications. Hence, significant errors can be expected in the subsequent phase retrieval process. While the simple flat field correction scheme by division is actually a crude approximation, it still works in some cases, whereas going terribly wrong in others. Figure 1 illustrates the basic problem investigated here. The inhomogeneities in $P$ cause distortions which cannot be divided out. Strong artifacts of the mirror system are still observed in the 'corrected' hologram of a polystyrene sphere. The goal of the present work is to investigate the errors of the common flat field correction. In which cases are they strong, and in which cases are they negligible? In a second step, algorithmic approaches beyond the simple empty beam correction are presented, and tested numerically as well as experimentally.

Simultaneous reconstruction of probing beam $P$ and object $O$ have been achieved by ptychographic algorithms [23, 24], based on the redundancy generated by lateral scanning with partial overlap. The method was first developed for far-field coherent diffraction data collected from a compact probe in the object plane [23, 24], but some recent generalizations to near-field (Fresnel) diffraction data have been demonstrated [25]. However, to this end $P$ had to be further scrambled by a wavefront diffuser in order to generate enough diversity. Further, for the case of an illumination by a Fresnel zone plate, special reconstruction schemes were devised [26], based on constraints in several planes including the pupil of the zone plate to define

#203649 - $15.00 USD Received 10 Jan 2014; revised 25 Mar 2014; accepted 30 Mar 2014; published 6 May 2014

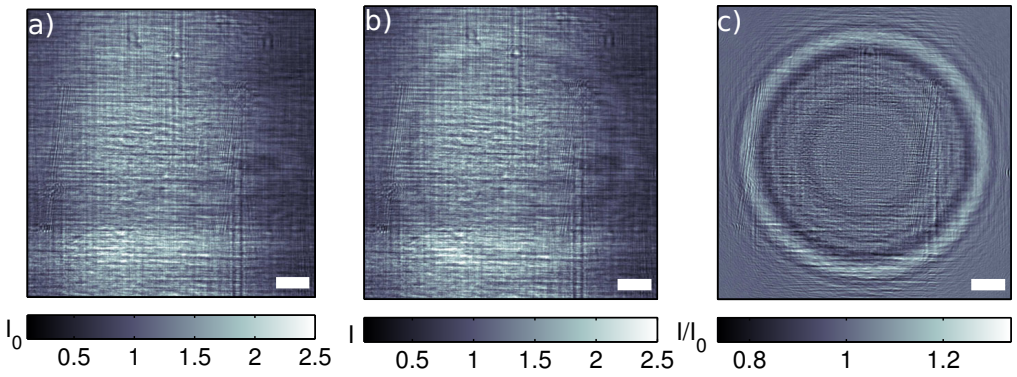


Fig. 1. Illustration of the flat field problem, for a $10\mu$m (diameter) polystyrene sphere positioned at a defocus distance of $z_1 = 10$ mm behind the focal plane of the KB mirror system at beamline ID22NI (ESRF, Grenoble), recorded at a detector distance of $z_1 + z_2 = 525$ mm and photon energy of $E = 17$ keV. (a) Empty beam recording showing the artifacts stemming from mirror imperfections. (b) Raw hologram of the sphere. (c) Corrected hologram as obtained by division of (b) by (a), i.e. the standard flat field or empty beam correction scheme. All data sets are normalized to the respective mean intensity. Scale bar of $2\mu$m indicates the corresponding distance in the object plane.

the probe's support. Unfortunately, both ptychography based on lateral scanning and the multi-plane Fresnel-CDI scheme [26, 27] turn out to be unsuited for the problem of the empty beam reconstruction in full field propagation imaging, since the necessary redundancy/diversity is generally not provided by lateral scanning. For a discussion of redundancy/diversity as well as of the sampling criteria relevant for ptychography, see also [28]. This is why we turn to an approach based on multiple detection planes in this work in order to reconstruct $P$. A multi-plane reconstruction scheme was first introduced in optics and electron optics in 1973 [29]. Since then this scheme and variations thereof have been used in microscopy to recover the complex valued point-spread-function (PSF) [30], and also in the field of x-ray imaging to reconstruct an exit wavefield $P \cdot O$ [31, 32]. However, in [31, 32] the multi-plane detection has not been used to recover $P$ itself, simultaneously with the object $O$, which is provided here. We therefore extend near-field imaging in a similar manner as ptychography has previously done for far-field coherent imaging [23, 24].

The manuscript is organized as follows: Section 2 further defines the problem of the wavefront distortions and the associated correction schemes. The notation and the basic concepts of the work are introduced. Section 3 presents the experimental setup and parameters. Section 4 presents a single distance approach for the reconstruction of $P$, which we denote as *divide&update*. Finally, we turn to the reconstruction of $P$ based on multiple detection planes in Section 5, before the paper closes with conclusions and outlook in Section 6.

## 2. How wrong is the standard empty beam correction?

Before we turn to reconstructions of $P$ let us address the validity of the standard empty beam correction, i.e. the approximation

$$|\mathscr{D}_z(O)|^2 \simeq \frac{|\mathscr{D}_z(P \cdot O)|^2}{|\mathscr{D}_z(P)|^2}, \tag{1}$$

#203649 - $15.00 USD Received 10 Jan 2014; revised 25 Mar 2014; accepted 30 Mar 2014; published 6 May 2014

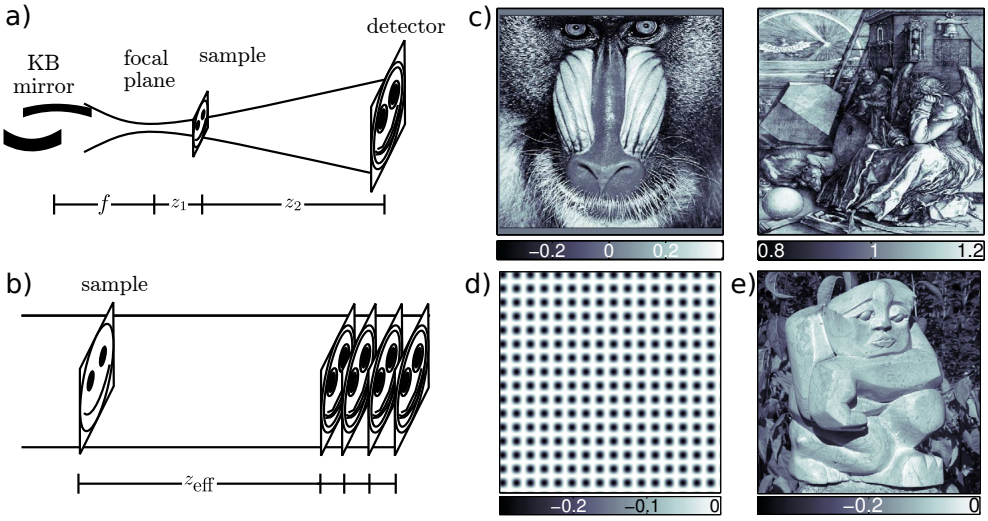


Fig. 2. (a) Sketch of the imaging scheme with the mirrors, the focus, the object and the detector. The probing beam $P$ is generated by a pair of KB-mirrors at the distance $f$ in front of the focal plane. The sample is placed at a distance $z_1$ behind the focal plane, and the sample to detector distance is $z_2$. (b) The equivalent parallel beam geometry corresponding to (a) with $z_{\text{eff}} = z_1 z_2/(z_1+z_2)$ and a geometrically reduced detection plane with $M = (z_1+z_2)/z_1$. (c) The phantom of $P$ used in the numerical simulations. A mandrill monkey image serves as the input for the phases, Dürer's Melencolia I as input for the amplitudes, both images are taken from MATLAB. The phases are in the range of [-0.4 0.4] rad and the amplitudes in [0.8 1.2]. The image size is $512 \times 512$ pixel. (d) The object $O$ used for the numerical simulations consisting of a phase shifting 2D sine grating, here shown for a periodicity of 32 px and a phase shift of -0.3 rad. (e) The test object used for multiple plane reconstructions. The image of a stone sculpture serves as phases. The phases are in the range [-0.4 0] rad, the amplitudes are uniformly 1, thus we have a purely phase shifting object.

where $\mathscr{D}_z$ denotes the Fresnel propagation over the propagation distance $z$, with coordinates defined in Fig. 2. $\mathscr{D}_z$ is given by

$$\mathscr{D}_z(\Psi) = \exp(i2\pi/\lambda z)\,\mathscr{F}^{-1}\left[\exp\left(-i\pi\lambda z(k_x^2+k_y^2)\right)\mathscr{F}(\Psi)\right], \tag{2}$$

where $\mathscr{F}$ denotes the Fourier transform, $\lambda$ the wavelength and $k_{x,y}$ the spatial frequencies. The correction according to Eq. (1) can be justified for point sources, or equivalently plane waves, see also appendix A. Only in idealized cases, the measured $|\mathscr{D}_z(P\cdot O)|^2$ can be written as $|\mathscr{D}_z(P)|^2\,|\mathscr{D}_z(O)|^2$. In all other cases in particular for $P$ resulting from focusing the x-rays to a finite spot size, $|\mathscr{D}_z(P\cdot O)|^2$ corresponds to a convolution of $P$ and $O$, and cannot be 'deconvoluted' by applying Eq. (1). Note that propagation of parallel and spherical wavefronts can be treated in the same way, after application of a simple variable transform introducing an effective defocus distance $z \to z_{\text{eff}} = z_1 z_2/(z_1+z_2)$ as well as a geometric magnification of the pixel size $M = (z_1+z_2)/z_1$ (Fresnel scaling theorem) [2]. For numerical calculation, the divergent (cone) beam case can therefore be easily transformed to an equivalent parallel beam case, see Fig. 2(b). By rearranging Eq. (1) we can introduce a metric $\delta$ to measure the error of the flat field correction

$$\delta = |\mathscr{D}_{z_{\text{eff}}}(O)|^2 - \frac{|\mathscr{D}_{z_{\text{eff}}}(P\cdot O)|^2}{|\mathscr{D}_{z_{\text{eff}}}(P)|^2}. \tag{3}$$

#203649 - $15.00 USD Received 10 Jan 2014; revised 25 Mar 2014; accepted 30 Mar 2014; published 6 May 2014

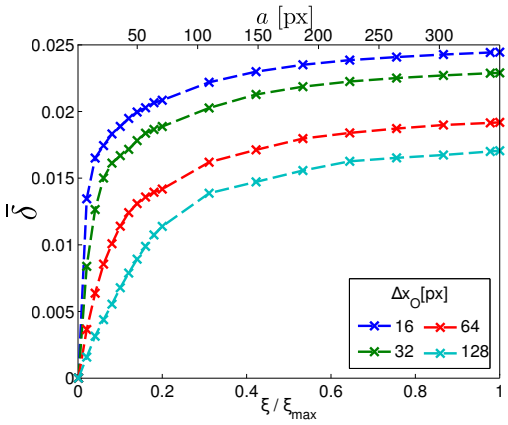


Fig. 3. The error $\bar{\delta}$ as function of the normalized cut-off frequency $\xi/\xi_{\max}$ in the filter applied to the probe $P$, for different periodicities $\Delta x_O$ (grid spacings). The alternative x-label on the top indicates the effective source size $a$ in units of pixels, corresponding to $\xi$. The simulation can be carried out in unit-less pixel variables and Fresnel numbers.

Since $\delta$ yields a matrix of errors, we use for our purposes $\bar{\delta}$ for the mean error over all pixels in the image in the simulations below:

$$\bar{\delta} = \frac{1}{N^2} \sum_{\text{all pixel}} \delta, \tag{4}$$

where $N$ is the number of pixels in one direction. In order to study the dependence of $\bar{\delta}$ on the geometric parameters, we perform a numerical simulation. The relevant parameters are the source size $a$ generating the probe $P$ and the characteristic length of the object $\Delta x_O$. To be able to work in the (numerically convenient) equivalent geometry of parallel beams, a correlation length of the probe $\Delta x_P$ is introduced, characterizing the smallest length scale on which $P$ shows variations. In other words $\Delta x_P$ quantifies the smoothness of the image representing $P$ cf. Fig. 2(c). Next, in view of the physical interpretation, we can relate $\Delta x_P$ to a source size $a$, since the correlation length is limited by diffraction

$$a(\Delta x_P) = \frac{z_1 \lambda}{2\Delta x_P}. \tag{5}$$

In the simulation we prescribe different $\Delta x_P$ by a Fourier filtering of $P$ according to $P_{\text{filt}} = \mathscr{F}^{-1}[\mathscr{F}(P) \cdot H(k_x, k_y)]$. Different filter kernels can be used, such as Gaussian, hat profile, etc. In fact the simulation results below are found to be very similar. Finally, we chose a rectangular filter

$$H(k_x, k_y) = \begin{cases} 1 & \text{if } \max(k_x, k_y) < \xi \\ 0 & \text{if } \max(k_x, k_y) \geq \xi \end{cases}, \tag{6}$$

with the cutoff parameter $\xi$ as the control variable. $\xi$ is related to the effective source size (in the divergent beam geometry) according to $a(\xi) = \frac{z_1 \lambda \xi}{2\pi}$. Stated differently, the filter is used to blur the probe $P(x,y)$, in order to make it appear more like a plane wave on local scales. With $\Delta x_P$ as the second control parameter, the error $\bar{\delta}$ can be studied for any chosen example of $P$ and objects $O$ of varied feature size in pixel units, such as a sine grating with periodicity $\Delta x_O$. Note that the filter kernel is not introduced to take the effect of partial coherence into account, which

#203649 - $15.00 USD Received 10 Jan 2014; revised 25 Mar 2014; accepted 30 Mar 2014; published 6 May 2014

are of course relevant but not considered here. We always assume a fixed phase relationship between different points on the wavefront, i.e. a spatially fully coherent but aberrated probe.

In the simulation, we then evaluate $\bar{\delta}$ for the probe phantom shown in Fig. 2(c), denoted as the mandrill-Dürer-probe, where the amplitudes of $P$ are given by the Dürer carving, and the phases by a mandrill monkey. The test object is chosen as a purely phase shifting object consisting of a sine grating with a grid constant (periodicity) $\Delta x_O$. Both probe and object are represented by a $N \times N$ matrices with $N = 512$. The error (of the conventional empty beam correction according to Eq. (4) is then evaluated for a constant Fresnel number $F = \Delta x^2/(\lambda z_{\text{eff}}) = 0.0015$, as a function of $\Delta x_O$ in the range from 16 px to 128 px and as a function of the filter cutoff $\xi$, which was varied in the range from $2\pi/(N\Delta x)$ to $\pi/\Delta x$, with $\Delta x$ the pixel size in the plane of the object. Note that this formulation in terms of the natural units of pixel units and Fresnel number has been chosen in view of the generality. The value of $F$ corresponds in particular to the following (experimental) parameters: $\lambda = 0.07$ nm, $\Delta x = 25$ nm, $z_1 = 6$ mm, $z_2 = 519$ mm and $z_{\text{eff}} = 5.93$ mm. Next, we note that the varied range of the filter cutoff parameter can be transformed to a range of $a$ from 0.34 px to 349.92 px, according to Eq. (5), evaluated for the above (experimental) parameters.

The expectation is that $\bar{\delta}$ increases when either the source size $a$ is increased, or the feature size $\Delta x_O$ is decreased. Figure 3 shows the simulation results for $\bar{\delta}$ for different $\Delta x_O$ as function of $\xi/\xi_{\text{max}}$, with $\xi_{\text{max}} = \pi/\Delta x$. The alternative x-axis label on the top indicates the corresponding $a$. As expected $\bar{\delta}$ decreases if the bandwidth decreases, i.e. if $P$ is filtered more strongly with a smaller cut-off frequency $\xi$. Furthermore, the error $\bar{\delta}$ is always larger for smaller grid parameters than for larger grid parameters. The smaller the structure, the more stringent is the requirement to keep the source size $a$ small or the correlation length of the wavefront aberrations $\Delta x_P$ large. From this we can infer that small structures in the object will not be transferred correctly after application of the empty beam division, while the contrast of larger objects may not suffer so much. Interestingly, the experimental example shown in Fig. 1 seems to be in contradiction to the simulation results. The hologram of a 10 $\mu$m sphere which is illuminated by a beam emanating from a KB-focus with 100 nm spot size should not be affected by artifacts due to empty beam division. The paradox is resolved by the fact that while the full width at half maximum (FWHM) of the focal spot is well below 100 nm, the KB focus is characterized by long tails which extend over several $\mu$m. It is these tails which render the effective source size too large for a 'clean' empty beam division. This conclusion has been validated experimentally by placing a pinhole with 1.4 $\mu$m diameter in the focal plane, which then results in a less disturbed, i.e. cleaner empty beam, see Fig. 4.

## 3. Experimental setup

The experiment was performed at the nano-focusing beamline ID22NI at ESRF (Grenoble) at a photon energy of 17 keV (0.0729 nm). The source size (FWHM of the focus of the KB-mirror-system [21]) was determined to be 67 nm(vertical) and 73 nm(horizontal), as measured by a fluorescence knife edge scan. The sample and detector stage can be moved within a defocus range of $0-300$ mm and $300-1500$ mm, respectively. A FReLoN HD 4m detector (ESRF) equipped with a LSO:Tb (20 $\mu$m) scintillator and an optical magnification scheme was used, with an effective pixel size of 756 nm. In the first configuration the detector was placed at $z_1 + z_2 = 525$ mm. The variation of $z_{\text{eff}}$ is achieved by placing the sample at different $z_1$. Figure 4 shows the measured intensity patterns recorded in this setup. The left column corresponds to the empty beam, the center to the raw hologram of a grid and the right column to the empty beam corrected hologram, for the data recorded without (top row) and with (bottom row) a 'cleaning' pinhole of 1.4 $\mu$m diameter positioned in the focal plane. $P$ and $P \cdot O$ were recorded quickly after each other, so that the flat field correction is not affected by temporal drifts.

#203649 - $15.00 USD Received 10 Jan 2014; revised 25 Mar 2014; accepted 30 Mar 2014; published 6 May 2014

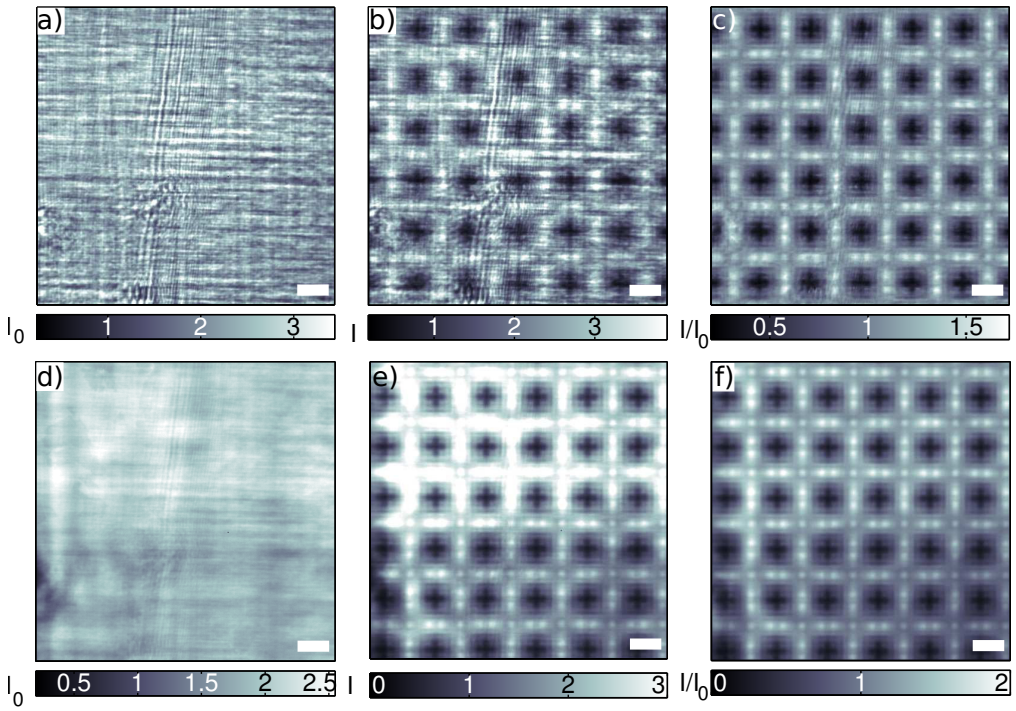


Fig. 4. Examples of images recorded for a gold grid test pattern with 1.5 $\mu m$ spacing at a defocus distance $z_1 = 26$ mm. (a) Empty beam measurement $P$. (b) Recorded (raw) hologram of $P \cdot O$.(c) Standard empty beam correction obtained by division of (b) by (a). (d), (e), (f) same as (a), (b), (c), but with a pinhole of 1.4 $\mu$m (diameter) inserted in the focal plane, which cuts the tails of the KB-beam, leading to a filtering of $P$. All data sets are shown after normalization to the average intensity. Scale bar indicates 2 $\mu$m in the sample plane.

In the second configuration the detector is moved and the sample (gold grid) is kept at a constant $z_1$ (25 mm). This approach also yields different $z_{\text{eff}}$ but the relative variation in $z_{\text{eff}}$ is much smaller if only $z_2$ is changed. The detector was placed at $z_2 = \{500, 501, 510, 600\}$ mm. For each distance 100 images with and without $O$ were recorded over a total of 40 minutes. Figure 5 shows data recorded using this configuration. Here, the time span between the measurements of $P$ and $P \cdot O$ was 20 minutes. This delay has visible influence on the quality of the flat field correction (c). Thus the primary prerequisite for the empty beam division is of course a stationary illumination field, or a correspondingly small sampling interval, in order to avoid temporal drift. While this trivial reason for possible artifacts is not our main concern, it does affect some of the experimental data. For this reason phase reconstructions run on data as Fig. 5(c) yield poor results as depicted in Fig. 5(d). The multiple detection plane reconstruction (Section 5) suffers also from this issue. For comparison, using data, collected over a considerably smaller time interval, as shown in Fig. 4(c) to run the phase reconstruction yields Fig. 7(c), as discussed further below. All relevant experimental parameters for the measurements shown are summarized in Tab. 1.

#203649 - $15.00 USD Received 10 Jan 2014; revised 25 Mar 2014; accepted 30 Mar 2014; published 6 May 2014

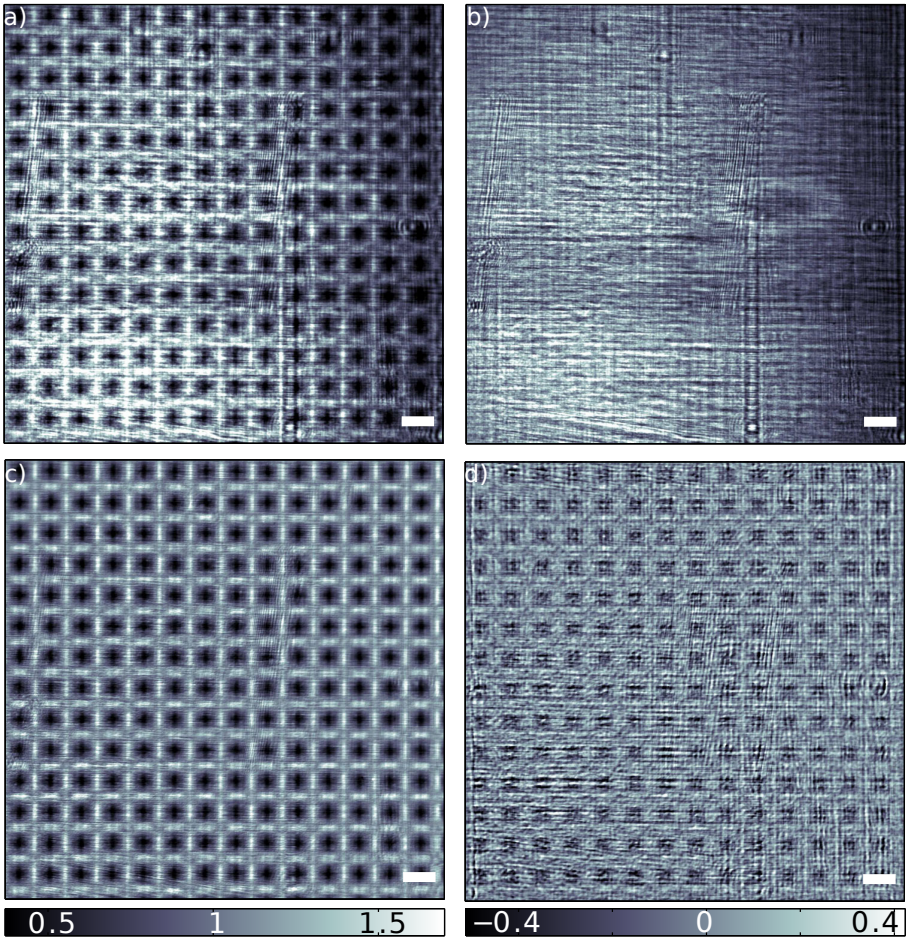


Fig. 5. Examples from a data set using the same object as in Fig. 4, but recorded in the detector scan ($z_2$ variation at fixed $z_1$). (a) Raw hologram of $P \cdot O$ for $z_2 = 510$ mm. (b) Corresponding empty beam $P$. (c) Empty beam correction: (a) divided by (b). (d) Phases of a reconstruction based on GS using (c) as measurement constraint and the projection on amplitude 1 and negative phases as sample constraint (cf. Section 4). (a), (b), (c) share the same colorbar shown below (c). (a) and (b) show the average of 100 measurements of the object and the empty beam, respectively, normalized by the mean intensity. Scale bar indicates 4 $\mu$m in the sample plane.

## 4. Reconstructions from a single distance

In order to overcome the errors involved with the conventional empty beam division, as illustrated above, we now turn to reconstruction strategies of $P$ and $O$. To this end, we use the common class of projection algorithms for the reconstruction [5], such as Gerchberg-Saxton (GS), Hybrid-Input-Output (HIO), Relaxed Averaged Alternate Reflection (RAAR) [33] etc. The algorithms were implemented using the SciPAL library [34] and are based on two alternating projections in two different planes: the projection $P_M$ adapts the current iterate of the wave

#203649 - $15.00 USD Received 10 Jan 2014; revised 25 Mar 2014; accepted 30 Mar 2014; published 6 May 2014

Table 1. Main parameters for the datasets shown in Figs. 1, 4, 5.

| | polystyrene sphere Fig. 1 | grid Figs. 4(a)–4(c) | grid pinhole Figs. 4(d)–4(f) | grid detector scan Fig. 5 |
|---|---|---|---|---|
| $\Delta x$[nm] | 14.4 | 37.4 | 37.4 | {36, 35.9, 35.3, 30.2} |
| $z_1$[mm] | 10 | 26 | 26 | 25 |
| $z_2$[mm] | 515 | 499 | 499 | {500, 501, 510, 600} |
| exposure time [s] | 0.5 | 0.1 | 0.1 | 0.1 |

field $\Psi$ to the recorded measurements in the plane of detection

$$P_M(\Psi) \equiv \mathscr{D}_{-z_{\text{eff}}}\left(\frac{\mathscr{D}_{z_{\text{eff}}}(\Psi)}{\left|\mathscr{D}_{z_{\text{eff}}}(\Psi)\right|}\sqrt{I}\right), \tag{7}$$

where $I$ denotes the measured intensities. The second projection $P_S$ acts in the plane of $O$ and can imply different constraints on $O$. For example positivity of the electron density variation, meaning $O$ implies negative phase shifts $\phi$ with respect to air/vacuum. $P_S$ could thus keep the negative $\phi$ and set all positive $\phi$ values of the iterate to zero. It can be formulated as

$$P_S(\Psi) \equiv \begin{cases} \Psi(\vec{x}) & \forall \phi(\vec{x}) \leq 0 \\ A(\vec{x}) \cdot \exp(i \cdot 0) & \forall \phi(\vec{x}) > 0 \end{cases}, \tag{8}$$

where $\vec{x}$ denotes the coordinates in the plane perpendicular to the propagation axis and $A$ the (reconstructed) amplitude at a given $\vec{x}$. Combinations of different constraints are also possible for example negative phase as well as a support constraint [17]. However, none of these constraints is sufficient for reconstruction of $P$ from a single intensity measurement, since (i) $P$ fills the whole field of view so that no compact support can be used, (ii) amplitudes and phases of $P$ are in the general case not proportional (coupled) or zero in any plane, and (iii) positivity may apply to the electron density which determines $O$, but figure errors of the mirrors can induce both positive and negative phases. Thus more information in form of additional measurements has to be used. The first idea which comes to mind is to bring a well known $O$ into the beam and take images with and without $O$. To this end, in the experiment a 200 nm gold grid with 3 $\mu$m period and 50% duty cycle (referred to as grid below) was used, see Figs. 4(a) and 4(b) for the measurements used in the reconstruction discussed further below. The basic principle of the algorithm for coupled reconstruction of $O$ and $P$ is sketched in Fig. 6(a). We will denote it as the divide&update (d&u) algorithm.

The right side of the sketch shows $P_M(\Psi_n^{P\cdot O})$ and $P_M(\Psi_n^P)$ where $n$ denotes the iteration index. The left side shows the update of $P$ and $O$. In order to obtain a separation of the exit wave field $P \cdot O$, we need an initial guess for $O$. A guess for $O$ is easily obtained by running a phase reconstruction step on the empty beam corrected measurements. One iteration of d&u starts with applying $P_M(\Psi_n^{P\cdot O})$ and $P_M(\Psi_n^P)$ on $P$ and $O$. $P_0$ and $(P \cdot O)_0$ (the initializations) are chosen with uniform amplitude 1 and phase 0. After application of $P_M(\Psi_n^{P\cdot O})$ we can use the guess of $O$ to obtain an update for $P$ (blue arrow). We likewise use $P_M(\Psi_n^P)$ to update $O$ (red arrow). The updated versions $O_{n+1}$ and $P_{n+1}$ are then used to compute the new exit wave $(P \cdot O)_{n+1}$ (green arrows). This concludes one iteration of d&u. In practice, a few enhancements were added to the algorithm, and several additional constraints were tested. First, in the spirit of hybrid input-output, the update $P_{n+1}$ is calculated as an average of $P_n$ and the update, same holds for $O_{n+1}$. Second, $O_{n+1}$ and $P_{n+1}$ were always projected on negative phases, see Eq. (8). We can consider this negativity (or positivity) constraint to be based on a physical relationship, such as

#203649 - $15.00 USD Received 10 Jan 2014; revised 25 Mar 2014; accepted 30 Mar 2014; published 6 May 2014

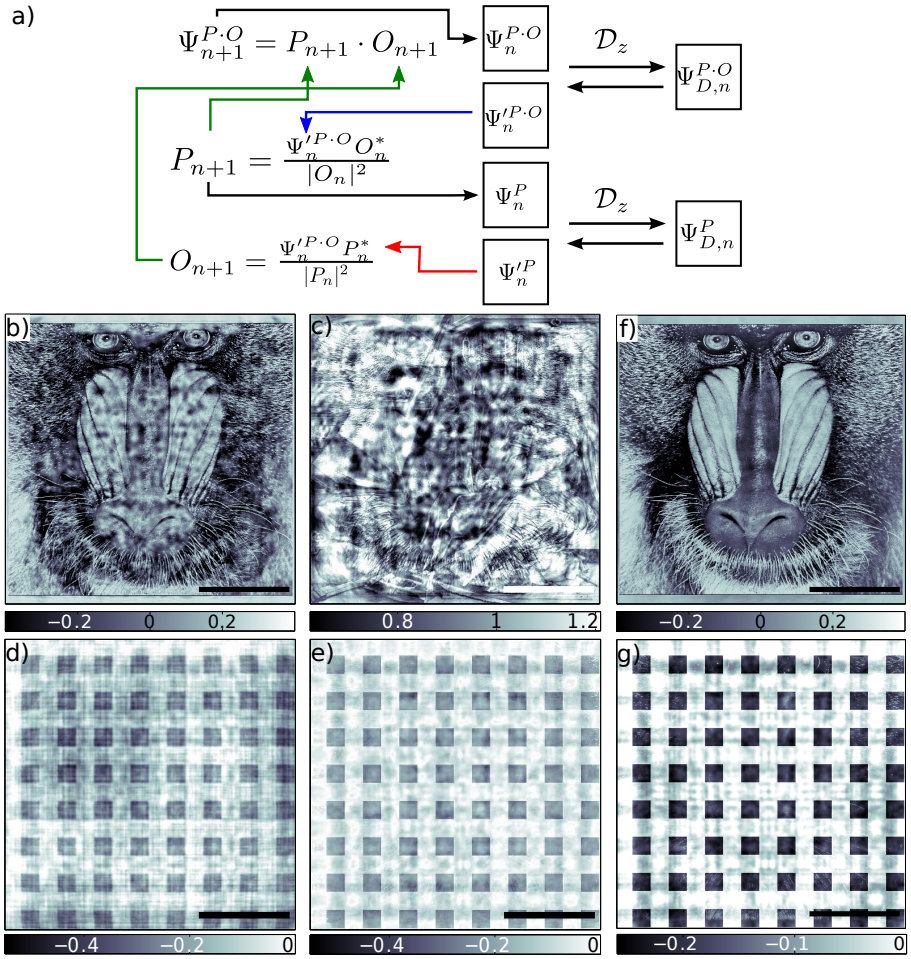


Fig. 6. Algorithm sketch for divide&update (d&u) and simulated reconstructions. (a) Principal sketch of d&u. Further explanations in Section 4. (b) Phases of the reconstructed mandrill-Dürer-probe and (c) corresponding amplitudes. (d) Phases of the first guess of $O$ as obtained by the GS algorithm applied to the empty beam corrected hologram. (e) Phases of $O$ after 200 iterations of d&u, showing the improvement by the nested update. (f) and (g) show reconstructions from a pure phase probe, i.e. a beam with phases represented by the mandrill image, and amplitudes equal to one (denoted as mandrill-1-probe). Besides the negative phase constraint also the projection to uniform amplitude is used. (f) Phases of $P$, amplitudes of $P$ not shown. (g) Phases of $O$ after 200 iterations of d&u. Scale bar indicates 4 $\mu$m.

#203649 - $15.00 USD Received 10 Jan 2014; revised 25 Mar 2014; accepted 30 Mar 2014; published 6 May 2014

positivity of the electron density (implying negativity of the object phase with respect to the vacuum wave). Therefore, one may be tempted to conclude that it would not hold for scattering length distributions which can change sign (as for neutrons), or for a sample embedded in a matrix. In the latter case the density of the object could be larger or lower than the matrix. Since a global phase offset is irrelevant, translating or reflecting all pixel values to negative or positive sign thus is not restrictive in our case, but is found to stabilize the algorithms by 'aligning' the phases. Finally, we projected $O$ to unit amplitude 1, implying the constraint for a purely phase shifting $O$.

### *4.1. Simulation results*

Figures 6 (b) and (c) show the result for the simulation of the d&u algorithm, after 200 iterations of d&u. The phantom used for $P$ is the mandrill-Dürer probe introduced in Fig. 2(c). While the reconstructed phases shown in (b) resemble the mandrill image, the reconstructed amplitudes (c) are far off the Dürer input and exhibit significant contaminations of the phase (mandrill image). Hence, the phases of $P$ are reconstructed to some extent, while the amplitudes are not. The object $O$, on the other hand shows a better quality, compare the result shown in (e) to the initial guess (d), which was computed from the standard empty beam corrected hologram by a GS-algorithm. The reconstruction in the d&u scheme is clearly better then the GS-solution which is spoiled by the wrongful empty beam division. However, the d&u result still shows residual cloudy artifacts, which show that the separation of $O$ and $P$ is not sufficient. If we use a purely phase shifting $P$ in the simulation and imply the corresponding constraint, the reconstruction quality is excellent, see the reconstructions of $P$ in (f), and of $O$ in (g), respectively. The amplitudes of $P$ are not shown but exhibit $\pm 15\%$ (max.) variations around 1. This variation is due to the fact, that the final reconstruction is generated after a last application of $P_M$, we use this procedure for every reconstruction.

### *4.2. Experimental data*

Figure 7 shows the d&u reconstruction of the experimental data recorded for the gold grid. Close inspection of the reconstructed phases of $P$ (a) show again regular structures which are artifacts stemming from the gold grid. The amplitudes of $P$ (b) look reasonable, with no bigger imprints of the grid. Here, the reconstruction quality cannot be improved significantly by assuming a constraint of coupled real and imaginary component of the index of refraction (dipersion and absorption correction), such as proposed in [35]. The results also do not improve if we take a second $z_1$ position for the same object into account such that two positions in the same $P$ are probed.

## 5. Reconstructions from multiple detector distances

The previous section has shown that images of the object and probe at a single distance do not fully constrain the reconstruction of $P$. We thus turn to an approach of using multiple measurements of the beam in parallel. By moving the detector coordinate $z_2$, the effective propagation distance $z_{\text{eff}}$ is modified both for $P \cdot O$ and the empty beam $P$, which is measured at each detector distance. This experimental setup is sketched in Fig. 8. For the geometry of high magnification, $z_2 \gg z_1$, $z_{\text{eff}}$ changes only very little with the variation of $z_2$, since for $z_2 \to \infty$, $z_{\text{eff}} \to z_1$. We use the multi-distance (multi-magnitude) projection algorithm proposed by Allen et al. [36] to reconstruct the wave fields. The algorithm is denoted as mmp (multi-magnitude projection) and is rather straight forward. It uses only the measurements in the different detection planes as constraints, with no constraint in the sample plane. Using 4 detection distances, we have

$$\Psi_{n+1} = P_{M_4}(P_{M_3}(P_{M_2}(P_{M_1}(\Psi_n)))) \,, \tag{9}$$

#203649 - $15.00 USD Received 10 Jan 2014; revised 25 Mar 2014; accepted 30 Mar 2014; published 6 May 2014

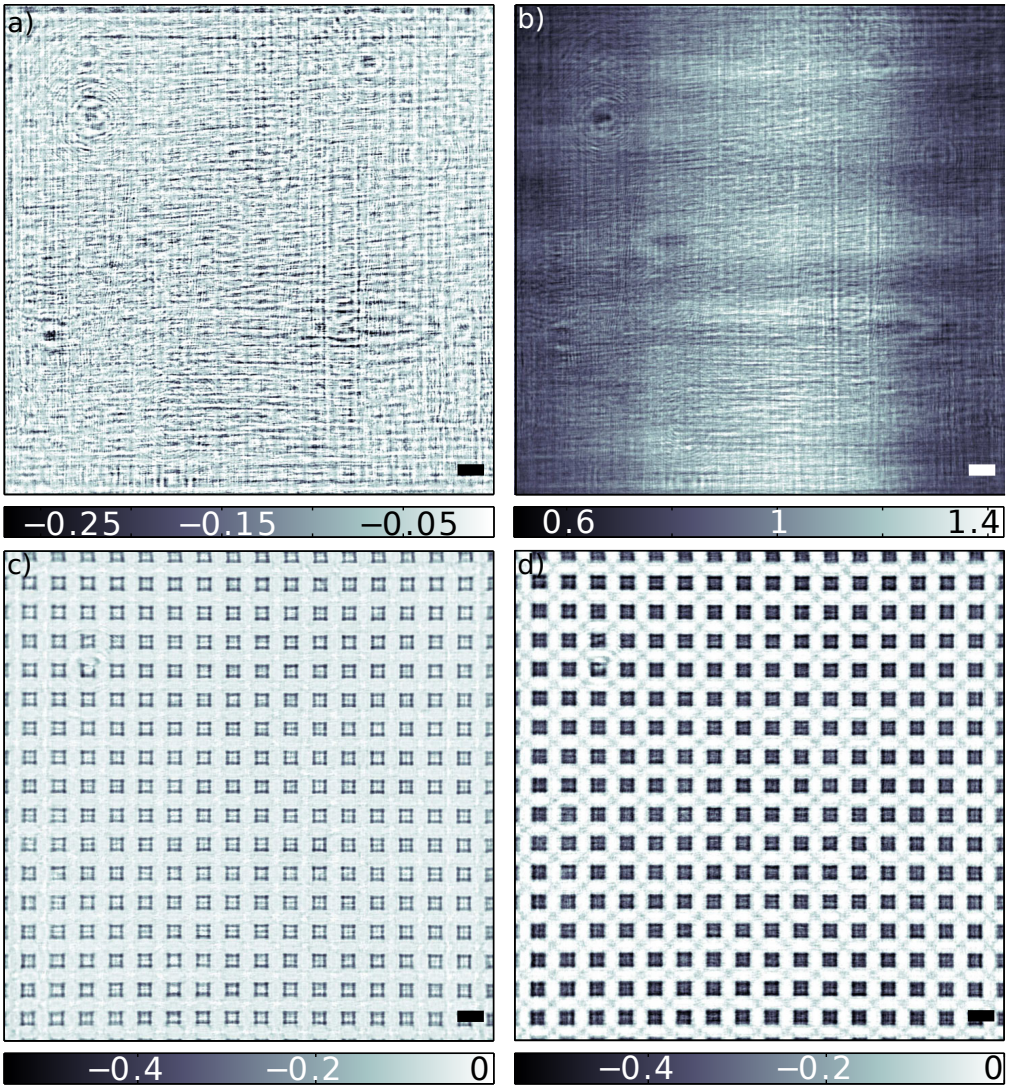


Fig. 7. Reconstructions of experimental data with the divide&update algorithm. (a) Phases and (b) amplitudes of the reconstructed $P$. (c) Phases of the first guess of $O$ (gold grid) as obtained by the GS algorithm applied to the empty beam corrected hologram. (d) Phases of $O$ after 200 iterations of d&u, clearly showing the improvement over (c). Scale bar indicates 4 $\mu$m in the sample plane.

where $P_{M_i}$ denotes the projection on the $i$-th measurement. We stress that no constraints on $O$ are used in the multi-plane algorithm. The algorithm has been used before in the literature to reconstruct the exit wave in x-ray imaging [37]. Instead of the sequential scheme implemented here, one could alternatively also update via an average over all detection planes, i.e. in a parallel manner [32]. mmp was demonstrated to be robust against noise, and can deal with first order phase jumps. But to our knowledge the algorithm has not been used for the reconstruction of $P$. We mention two small deviations from the original algorithm (i) the measurements are not equally spaced (ii) $P_M$ brings $\Psi$ always back in the plane of $O$ before projecting on the next

#203649 - $15.00 USD Received 10 Jan 2014; revised 25 Mar 2014; accepted 30 Mar 2014; published 6 May 2014

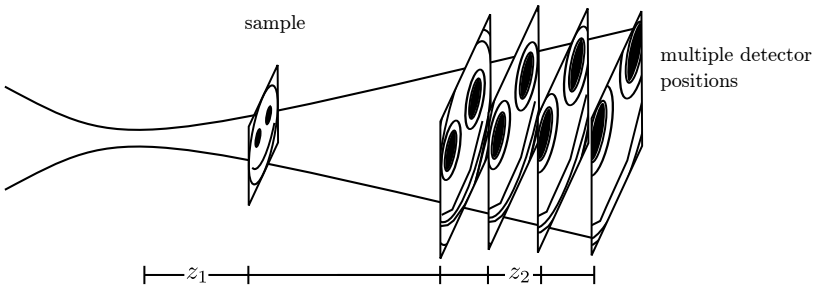


Fig. 8. Detector distance variations. In this approach $z_2$ is varied and $z_1$ is kept constant.

measurement. The original implementation projects directly on the next measurement.

### *5.1. Simulation*

The simulated reconstruction was carried out for the same four detector distances as in the experimental case discussed below, but in the equivalent (parallel beam) geometry with $z_{\text{eff}} = \{23.810, 23.812, 23.832, 24\}$ mm. Poisson noise was added to each pixel of the simulated holograms of $P$ and $P \cdot O$ for an expected number of $10^9$ detector photons. For $P$ the mandrill-Dürer-probe was used as above. For the phase of $O$, the image of a stone sculpture was used with phases in the range of [-0.4 0] rad, see Fig. 2(e). Amplitudes of $O$ were set to 1 (purely phase shifting object).

Figure 9 shows the simulation results for 1000 mmp iterations. The reconstructed phases and amplitudes of $P$, as shown in (a) and (b), respectively, are in very good agreement with the phantom, see Fig. 2(c). The amplitudes show only a faint imprint of the phases. The reconstruction of $P \cdot O$ (c) and (d) is also very good, and illustrates the fact that the exit wavefield is dominated by $P$, which corresponds to the case of a heavily aberrated probe. The information on $O$ is visible only in form of contours of the stone sculpture in the phases. Dividing the recovered $P \cdot O$ by $P$ finally yields $O$ (e) and (f), again of very good quality, cf. Fig. 2(e). The phases of $O$ shown in (e) also only expose a faint imprint of the mandrill's whiskers. The amplitudes of $O$ show an imprint of the phases of $P$ and $O$ but the distortions are only in the range of $\pm 10\%$ (max.). The error metric $\Delta$ on the reconstructions is defined by

$$\Delta = \frac{1}{N^2} \sum_{\forall \text{pixel}} |\text{original} - \text{reconstruction}| \,, \tag{10}$$

where $N^2$ is the number of pixels, and is given in the titles of the sub-figures for each reconstruction. We notice that $\Delta$ is about 3 times larger for the phase reconstructions than for the amplitude reconstructions. Also the reconstruction of $P \cdot O$ has a higher error value than the one of $P$. The reconstruction results and error values are already quite good, despite the small changes in $z_{\text{eff}}$ (corresponding to the experimental values). As expected, the simulations show that by choosing propagation distances with more variation in $z_{\text{eff}}$ (translational diversity) the errors can be further decreased by several orders of magnitude. The challenge is therefore clearly to cover a sufficient $z_{\text{eff}}$ range in the experimental implementation.

### *5.2. Experimental data*

Motivated by the successful numerical results, the next step was to apply the mmp algorithm to experimental data. The data was recorded in the second configuration as described in Section

#203649 - $15.00 USD Received 10 Jan 2014; revised 25 Mar 2014; accepted 30 Mar 2014; published 6 May 2014

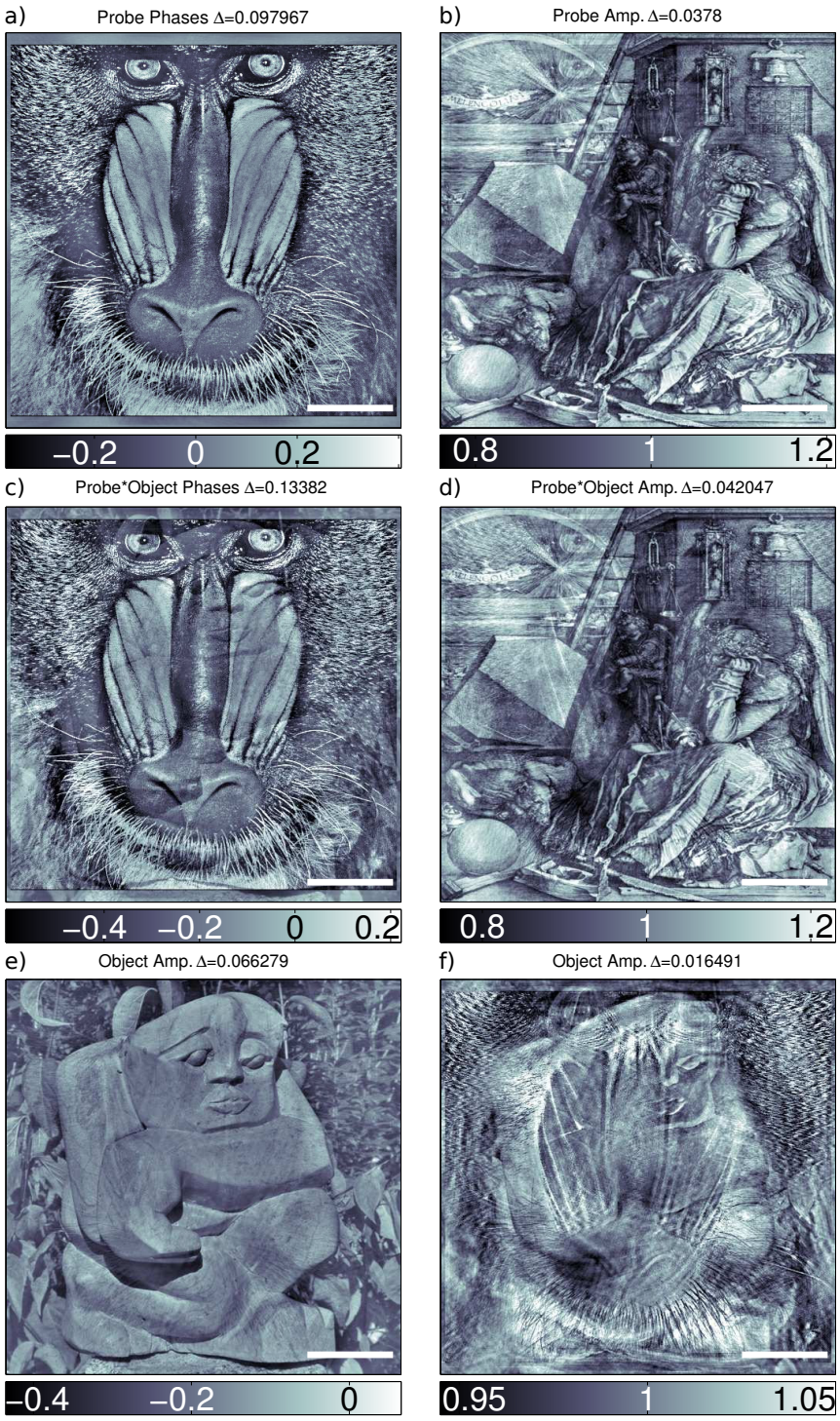


Fig. 9. Reconstruction of the simulated detector scan experiment with 4 distances using the multiple magnitude projection algorithm (Eq. (9)). The left column shows phase and the right column shows amplitude. (a), (b) Reconstructed $P$. (c), (d) Reconstructed $P \cdot O$. (e), (f) Reconstructed $O$, from division of $P \cdot O$ by $P$. The $\Delta$ in the title denotes the reconstruction error as defined in Eq. (10). Scale bar indicates 4 $\mu$m in the sample plane.

#203649 - $15.00 USD Received 10 Jan 2014; revised 25 Mar 2014; accepted 30 Mar 2014; published 6 May 2014

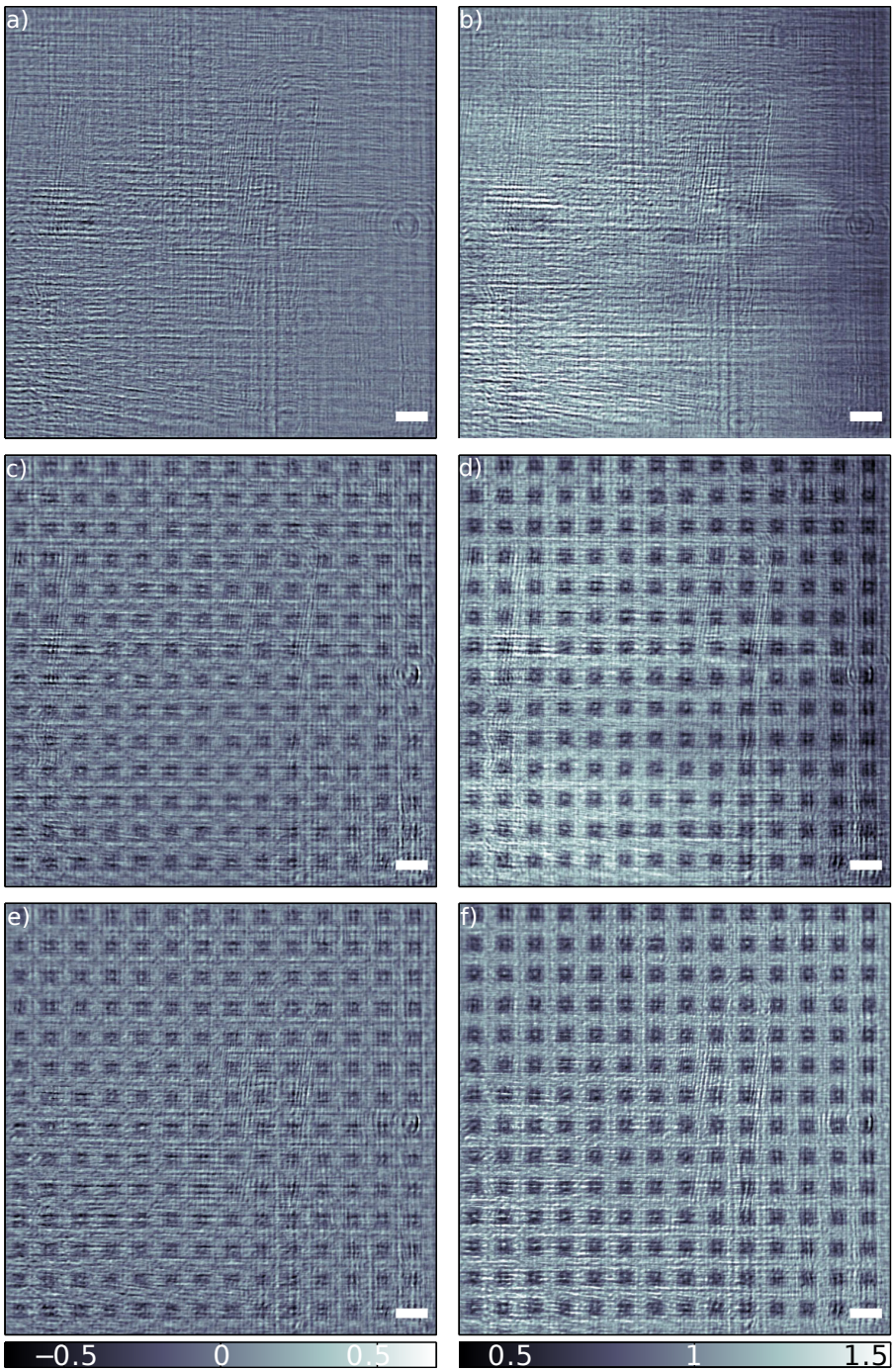


Fig. 10. Reconstruction of the experimental detector scan with the multiple magnitude projection algorithm (Eq. (9)). The left column shows phase and the right column shows amplitude of the reconstruction. (a), (b) Reconstructed $P$. (c), (d) Reconstructed $P \cdot O$. (e), (f) Reconstructed $O$, from division of $P \cdot O$ by $P$. The pixel size is 36 nm. The colorbar below the last image in a column applies to all images of the column. Scale bar indicates 4 $\mu$m in the sample plane.

#203649 - $15.00 USD Received 10 Jan 2014; revised 25 Mar 2014; accepted 30 Mar 2014; published 6 May 2014

3, exemplary data is depicted in Fig. 5. Due to the cone beam geometry and different magnifications the recorded images must be rescaled and aligned. The images were cropped to the smallest field of view. We have reconstructed the two data sets with and without $O$ independently.

Figure 10 shows the results of the reconstruction of experimental data. The reconstructions of phase and amplitude of $P$ are shown in (a) and (b), respectively. The result looks similar but more plausible than the reconstruction of $P$ in Figs. 7(a) and 7(b). Comparing the reconstruction of $P$ and $P \cdot O$ in (c) and (d) we can also identify the same structures in both, which indicates that the reconstructions are consistent. However, when extracting $O$ from the reconstruction of $P \cdot O$ by dividing by $P$, certain artifacts remain, and the result looks worse than the result for $O$ reconstructed from a single distance as before in the d&u approach, shown in Fig. 7(d). This is attributed to the fact that this data set is more affected by temporal drift of $P$, simply because the delay between measuring $P$ and $P \cdot O$ was much too long, namely about 20 min. It is surprising that the reconstruction of $P$ is still possible at this point. For an optimized scan, a time interval between subsequent images of less than a minute is realistic, in view of the necessary detector movement. This could sufficiently avoid drift of $P$ and enable reconstructions of similar quality as those in the numerical simulation.

## 6. Summary and Conclusion

The first aim of this work was to illustrate the problems associated with the standard flat field correction, both numerically and with experimental data. To this end, we have used an error metric $\delta$ Eq. (4). We have investigated, under which conditions the division of intensity images of $P$ and $P \cdot O$ in the detection plane is a sufficient approximation, in terms of object and source size. From the simulation we can conclude that the reconstruction of the probe $P$ is an important step towards higher resolution in propagation imaging, since otherwise good data quality can only be expected for feature sizes much larger than the source size.

As a first attempt, we have presented 2 algorithms to reconstruct the empty beam $P$ in x-ray propagation imaging. The first algorithm d&u, devised for a single distance data set, uses a nested scheme to update $P$ and $O$. This scheme works well for purely phase modulated $P$ and $O$, but it breaks down for the general case of an amplitude and phase modulated $P$. We have also inferred from this approach that it is not sufficient to use one image of $P$ and $P \cdot O$ each, even if $O$ is known. The second algorithm mmp is already known in literature but has not been used to reconstruct $P$. The algorithm requires multiple distance measurements of $P$. mmp yields good reconstructions in simulations even for noisy data with small variation in $z_{\text{eff}}$. In order to probe $P$ at different distances in the experiment, the sample-detector distance $z_2$ was changed, which is intrinsically different from changing the sample position $z_1$. Analyzing this data set showed that in order to get a good reconstruction of $P$ the time between measurements should be short. This is of course also well known for the standard empty beam correction. However, in order to cover a sufficient diversity (range in Fresnel numbers), the detector has to be moved over a rather wide range, which makes this approach more prone to temporal drift. Flight tubes are another experimental difficulty in implementing this approach, unless the detector is contained in the flight tube. For the experimental strategy, the number of detector positions and the shift $\delta z_2$ must be optimized in view of sufficient diversity while keeping the total measurement time as small as possible in view of drift elimination. Interestingly, a recent generalization of ptychography to longitudinal scanning (OAP, on-axis ptychography) has also shown, that a defocus scan with constant detector position, i.e. moving only the sample, is not sufficient for simultaneous reconstruction of $P$ and $O$ [38]. However, numerical simulations have yielded good results already for two detector distances. This still awaits experimental verification, but it can be anticipated that more than one algorithm will be suitable to perform the simultaneous

#203649 - $15.00 USD Received 10 Jan 2014; revised 25 Mar 2014; accepted 30 Mar 2014; published 6 May 2014

reconstruction $P$ and $O$.

## 7. Appendix A

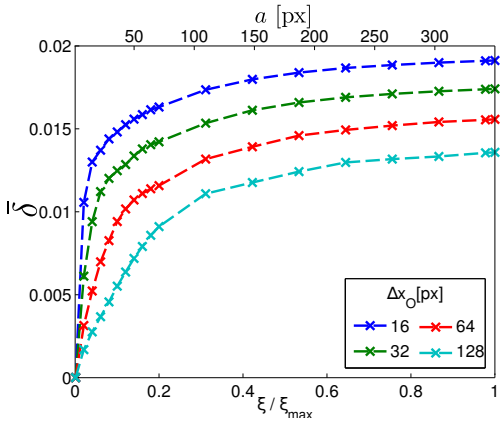


Fig. 11. The mean error of Eq. (11) as a function of the normalized cut-off frequency $\xi/\xi_{\max}$ in the filter applied to the probe $P$, for different periodicities $\Delta x_O$ (grid spacings). The alternative x-label on the top indicates the effective source size $a$ in units of pixels, corresponding to $\xi$.

The error of the standard flat field correction can be analyzed based on a rigorous mathematical proof starting from the stationary wave equation and resulting in an upper bound for the error as a function of all relevant parameters. This result will be presented elsewhere [39], and used an alternative definition of the error metric

$$\delta = \frac{\|\mathscr{D}_{z_{\text{eff}}}(P\cdot O) - \exp\left(-i2\pi/\lambda z_{\text{eff}}\right)\mathscr{D}_{z_{\text{eff}}}(O)\mathscr{D}_{z_{\text{eff}}}(P)\|_\infty}{\|\mathscr{D}_{z_{\text{eff}}}(P)\|_\infty \|\mathscr{D}_{z_{\text{eff}}}(O)\|_\infty}\,, \tag{11}$$

which differs from the heuristic expression given in Eq. (4). The numerator of $\delta$ measures the difference of $\mathscr{D}_{z_{\text{eff}}}(P\cdot O)$ and the product $\mathscr{D}_{z_{\text{eff}}}(O)\mathscr{D}_{z_{\text{eff}}}(P)$. This difference is then normalized by the modulus of the propagated $P$ and $O$. It is shown in [39] that the supremum of Eq. (11) is bounded by

$$\frac{\sqrt{2}\, z_{\text{eff}}\, \lambda}{8\,\pi\,\Delta x_P\,\Delta x_O}\,\frac{\int_{\mathbb{R}^2}|\mathscr{F}(P)|\mathrm{d}k\ \int_{\mathbb{R}^2}|\mathscr{F}(O)|\mathrm{d}k}{\|\mathscr{D}_{z_{\text{eff}}}(P)\|_\infty |\mathscr{D}_{z_{\text{eff}}}(O)\|_\infty}\,. \tag{12}$$

Figure 11 shows the results obtained with the metric Eq. (11). The simulation was carried out, following the same procedure as described in Section 2 also using the same set of parameters. Both errors Fig. 3 and Fig. 11 show the same behavior, regarding the strength of filtering ($\xi/\xi_{\max}$ varied) and the variation of object periodicity $\Delta x_O$. In fact it is possible to define several other metrics, showing the same general behavior as here, but without the mathematical foundation as Eq. (11).


### Acknowledgments

We thank Matthias Bartels, Martin Krenkel and Markus Osterhoff for help at the beamtime, and also for numerous discussions and fruitful collaboration in related projects. Funding by SFB 755 *Nanoscale Photonic Imaging* is gratefully acknowledged.